ARTICLE

Multiresponsive Microactuator for Ultrafast Submillimeter Robots

Xusheng Hui, Jianjun Luo,* Rong Wang, and Hao Sun

Cite This: https://doi.org/10.1021/acsnano.2c12203

Read Online

ACCESS | Metrics & More | Article Recommendations | Supporting Information

ABSTRACT: Untethered submillimeter microrobots have significant application prospects in environment monitoring, reconnaissance, and biomedicine. However, they are practically limited to their slow movement. Here, an electrical/optical-actuated microactuator is reported and developed into several untethered ultrafast submillimeter robots. Composed of multi-layer nanofilms with exquisitely designed patterns and high surface-to-volume ratios, the microrobot exhibits flexible, precise, and rapid response under voltages and lasers, resulting in controllable and ultrafast inchworm-type movement. The proposed design and microfabrication approach allows various improved and distinctive 3D microrobots simultaneously. The motion speed is highly related to the laser frequency and reaches 2.96 mm/s (3.66 body length/s) on the polished wafer surface. Excellent movement adaptability of the robot is also verified on other rough substrates. Moreover, directional locomotion can be realized simply by the bias of the irradiation of the laser spot, and the maximum angular speed reaches 167.3°/s. Benefiting from the bimorph film structure and symmetrical configuration, the microrobot is able to maintain functionalized after being crashed by a payload 67 000 times heavier than its weight, or at the unexpectedly reversed state. These results provide a strategy for 3D microactuators with precise and rapid response, and microrobots with fast movement for delicate tasks in narrow and restrictive scenarios.

KEYWORDS: microrobot, microactuator, multiresponsive, microelectromechanical systems (MEMS), nanofilms
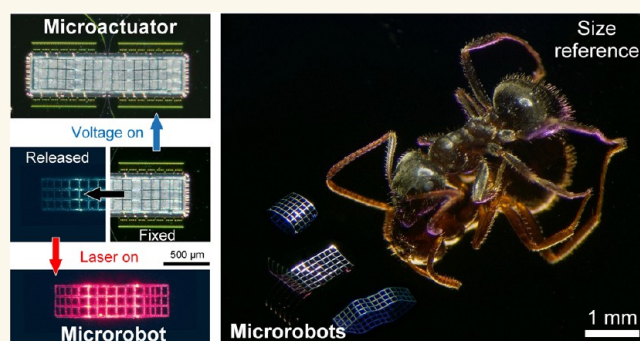
Microactuators that can convert multiple external stimuli into mechanical deformation and movement have attracted a great deal of attention for their potential in sensors, artificial muscles, microrobotics, and so on. As one of the most important promising applications of microactuators, untethered microrobots can perform delicate tasks in narrow spaces that would otherwise be impossible to access for large-scale robots. Therefore, they have shown significant potential in environment monitoring,[1] reconnaissance,[2] and especially in biomedicine (i.e., drug delivery,[3,4] disease diagnose,[5] targeted therapy,[6,7] cell and gene engineering,[8,9] in vivo biopsy,[10,11] and noninvasive surgery[12]). Compared with other existing tethered medical devices and robots, untethered microrobots exhibit better adaptability to access complex and narrow regions of the human body such as the heart,[13] brain,[14] and eye.[15] The benefits that come along with the application of these microrobots will be not only the reduction of trauma, recovery period, and infection risks to the patients but also the emergence and development of next-generation effective therapies. The minisize and the application scenarios of the microrobots require the ability to respond to external stimuli from the environment instead of wired and on-board energy supply. Nature-inspired biomimetic microrobots sensitive to chemical solutions,[7,16] ultrasound waves,[17,18] magnetic fields,[4,5,9,19,20] and light[21−24] have emerged and become a popular research topic. However, without the stability and controllability of tethered approaches, it is difficult for the speed of the most untethered microrobots to exceed 1 body length per second (1 BL/s). Therefore, there remain great challenges in improving the motion performance of untethered microrobots.

As a complex system, the motion performance of untethered microrobots is influenced by various aspects of factors. One of the most important reasons comes from the inherent physical and chemical limitations between the mechanical properties of the actuator materials, the actuation mechanism, and the design defects.[25] For example, the necessary duration required
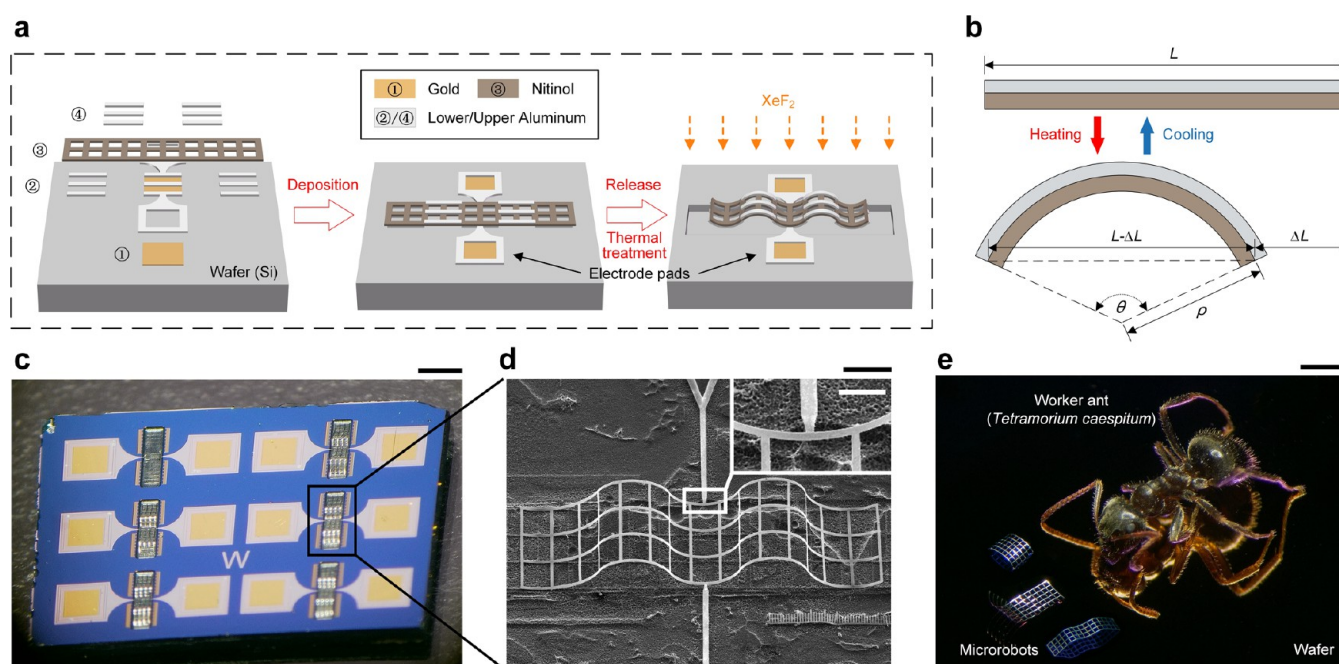
Figure 1. Design scheme and prototypes. (a) Schematic illustration of the structure of the microactuator. Left: exploded view of the microactuator which is composed of four layers (Numbers 1 to 4 from the bottom to top) of patterned films. Middle: the 2D shape of the microactuator, which sticks tightly to the wafer surface after sequential deposition. Right: 3D wavy structure of the microactuator after release in the XeF$_2$ atmosphere and heat treated. (b) Definition of the bending deformation of the bimorph strips. (c) 6 microactuators on a wafer slice (1.5 cm × 1.0 cm). (d) SEM photo of the 3D microactuator. The internal illustration captured the detail of the "weak link" between the microactuator and the electrode pads. (e) Optical microphotograph for size comparison between untethered microrobot prototypes and a worker ant (*Tetramorium caespitum*), which has a typical length of 2.6−4 mm. Scale bars: (c) 1 mm, (d) 200 μm, inset image 50 μm, (e) 1 mm.

for chemical reactions limits the performance of robots that respond to solvents. Not to mention the mechanical properties of hydrogel,[26,27] liquid crystalline polymers,[28] gel,[29,30] and paraffin wax,[23,24] which sacrifice responsiveness speed for higher flexibility. Among all the variety of actuator materials and actuation mechanisms, bimorph thin-film structures based on thermal deformation are considered most likely to be able to accommodate both flexibility and response speed.[31,32] In addition, thermal deformation can be easily combined with untethered actuation methods such as lasers. For example, Han et al. constructed 3D microactuators and microrobots through the SMA/PI bimorph film structure and optical-thermal mechanism.[33] The maximum actuation frequency and the motion speed exceed 10 Hz and ~0.4 BL/s, respectively. Another factor that could determine the motion performance of the microrobot is its movement pattern. Inspired by the diversity of animals and arthropods in nature, a variety of bionic microrobots have been developed such as multilegged,[34] earthworm-like,[35] and inchworm-like robots.[28] The proper bionic motion pattern of microrobots, which considers the actuation performance of the actuators and give full play to the efficiency to convert deformation into movement, is crucial to the motion performance. Inchworm-type motion is one of the most popular motion patterns for microrobots due to its simplicity and efficiency. However, it remains a great challenge to fabricate highly customized 3D microstructures for active anisotropic friction. Therefore, it is very difficult to modulate friction at the microscopic scale. Many inchworm-type microrobots are only able to move on ratchet surfaces, which supply unidirectional friction.[28,29,36] In summary, ultrafast and controllable untethered microrobots require a perfect balance

between the actuator structure, the actuation mechanism, the motion pattern, and the microfabrication technology.

Herein, electrical/optical-actuated 3D microactuators and untethered submillimeter 3D robots are reported. The microactuator is obtained through the sequential deposition of multilayer patterned nanofilms. Based on the thermal deformation of bimorph strips, the microactuator is capable of producing a precise response to voltages and lasers through the electrothermal and photothermal mechanisms, respectively. On the basis of high flexibility and precision, the structural temperature of the microactuator remains low (≤52 °C), which lowers the threshold for their applications. Benefiting from the small thickness of the nanofilms, a high surface-to-volume ratio of the microactuator enables an extremely fast heating and cooling rate for rapid dynamic response performance (up to 100 Hz). Inspired by the inchworm locomotion modes, the microactuator transforms into an optical-actuated untethered microrobot immediately after disconnection from the electrodes for complete freedom. The proposed design method and microfabrication technology allow us to access parallel fabrication of microrobots with multiple 3D configurations by simply changing the 2D layouts of each film. These microrobots exhibit excellent motion performance on various substrates. Highly related to the laser frequency, the maximum speed on the polished wafer surface reached 2.96 mm/s (3.66 BL/s) at 30 Hz. We also developed the control strategy for the directional motion of the microrobots. By offsetting the laser irradiation position from the center, clockwise/counterclockwise rotation can be realized. The proposed microrobots also possess excellent robustness against impacts and perturbations. They can remain functionalized after being reversed or crushed
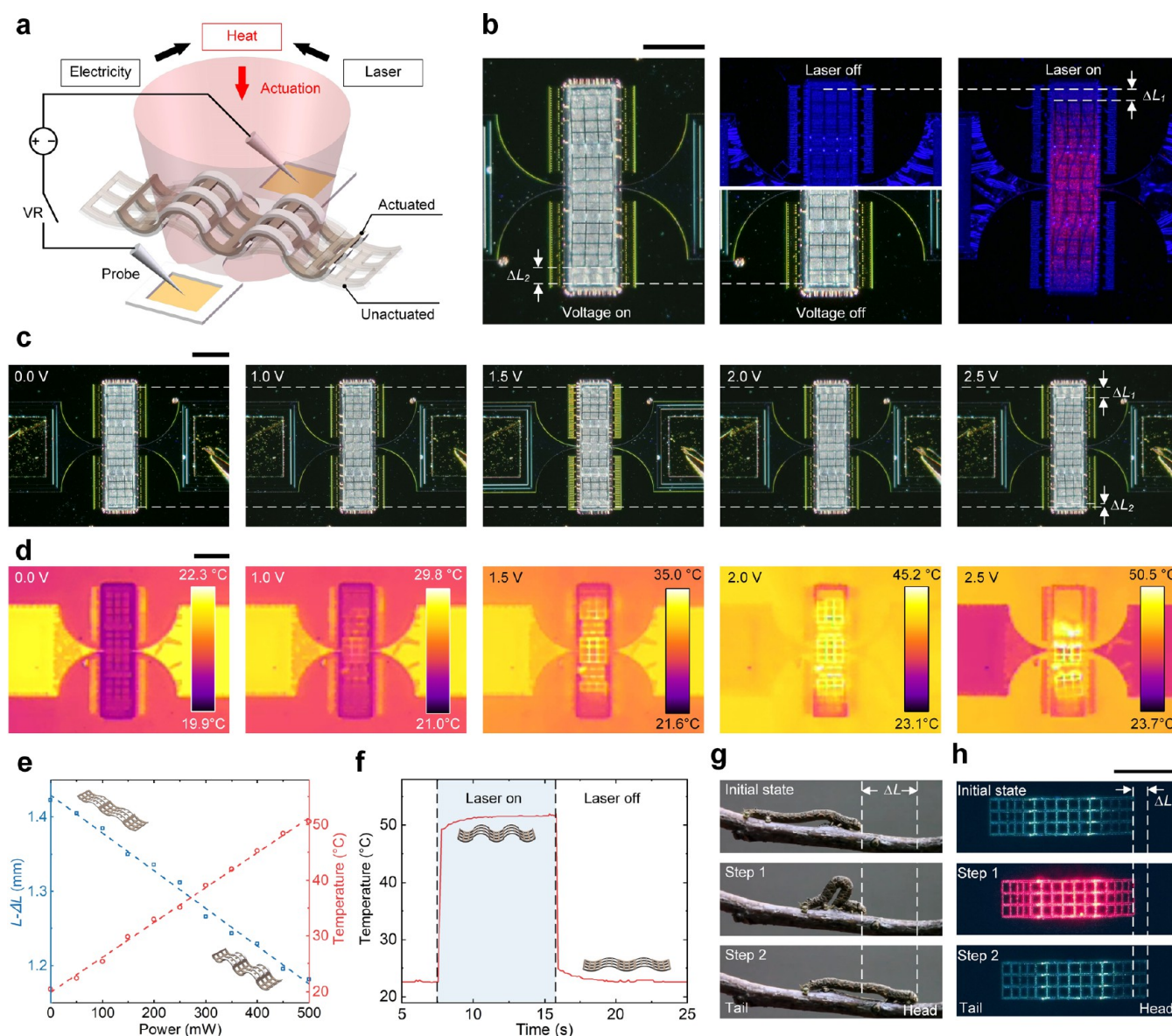
Figure 2. Actuation performance. (a) Schematic illustration of the electrothermal and photothermal actuation mechanism through electricity and laser of the microactuator. (b) Initial state (middle) and contraction deformation of the microactuator after applying voltage (left) and laser (right, an optical filter is added for better observation in intense lasers). (c) Steady-state response of the microactuator under DC voltages from 0.0 to 2.5 V. The dashed lines compare its projection length between 0.0 and 2.5 V. (d) IR camera images of the microactuator viewed from the top under DC voltages from 0.0 to 2.5 V. (e) Length-temperature-laser power graph of the microactuator in in situ tests. (f) Variation of the temperature of the microactuator after the laser was on and off. (g) Illustration of the crawling motion of the inchworm in nature. (h) Inchworm-type motion of the microrobot in this work. Scale bars: 500 μm.

by a load 67 000-times its own weight. The microrobot and its actuation method are also verified to be feasible in the retina surgery scenario where the light path is strictly limited. The proposed microactuators and microrobots will have broad application prospects in biomedical, environmental monitoring, and other fields.

RESULTS AND DISCUSSION

Design Scheme. The microactuator is obtained by the sequential deposition of several patterned nanofilms: a layer of gold film, two layers of aluminum films, and a layer of nitinol film. To fabricate the microactuators, a series of MEMS manufacturing methods, such as the magnetron sputtering process, the electron beam (E-beam) evaporation process, the

inductively coupled plasma chemical vapor deposition (ICPCVD) process, the photoresist lift-off process, and the isotropic vapor phase etching process of silicon, are involved. The detailed microfabrication method through MEMS is illustrated in Figure S1.

Figure 1 shows the scheme and prototype of the microactuators and microrobots. As shown in Figure 1a, the nitinol frame is a rectangular film with square holes to enlarge the deformation amplitude and facilitate the XeF$_2$ etching process. Aluminum films are parallel strips, which are deposited on the bottom and top surfaces of the nitinol film, forming several local bimorph strips. The main advantages of this metal couple are (1) that large difference in coefficients of thermal expansions (CTEs) leads to the significant deformation of the microactuator and microrobots, (2) that it can be

easily machined into high-quality nanofilms for rapid heat dissipation and response, (3) that the low electrical resistivity and optical reflectivity of aluminum facilitate the effective absorption of energy, (4) that good oxidation resistance of the nickel base alloys and the dense oxide film on the aluminum protects the microactuator and microrobot from damage during the etching process, and (5) that these two materials exhibit good biocompatibility. The hollow squares in the lower aluminum film form a pair of electrode pads along with the bottom gold film for electrical actuation. The microactuator remains in its 2D shape after microfabrication and sticks tightly to the wafer surface. After being released and heat-treated at 200 °C for 1 h, the temperature difference will lead to the bending deformation of the bimorph structures due to the mismatch of the CTEs of the different materials (Figure 1b). The thickness of these films is about several hundred nanometers. Therefore, it is reasonable to take these bimorph strips as thin plates that satisfy Kirchhoff's assumptions. Therefore, for a bimorph strip under uniform heating,

$$\rho = \frac{t\left[3(1+m)^2 + (1+m)\left(m^2 + \frac{1}{mn}\right)\right]}{6(1+m)^2(\alpha_2 - \alpha_1)(T - T_{env})} \qquad (1)$$

where ρ is the radius of curvature of the bimorph strip, t is the total thickness of the bimorph strip, m is the ratio of the thickness of these two films, n is the ratio of Young's modulus of the two materials, α_1 and α_2 are the coefficients of the thermal expansion of the two materials, T is the structural temperature of the bimorph strip, T_{env} is the temperature of the environment:

$$L - \Delta L = \rho\sqrt{2\left(1 - \cos\frac{L}{\rho}\right)} \qquad (2)$$

where L is the initial length of the bimorph strip, and ΔL is the change in the projection length. The microfabrication process in Figure S1 operates in a parallel mode, which allows a large number of microactuator samples to be processed simultaneously (Figure 1c). The SEM photo in Figure 1d shows the wavy 3D shape of the microactuator after release. There exists a "weak link" between the microactuator and the electrode pads for easier separation. After disconnection, the microactuator will be transferred to a plane for untethered movement. To provide a size comparison, the microrobot prototypes were positioned alongside and photographed with a worker ant (*Tetramorium caespitum*) (Figure 1e, Movie S1) and a coin (Figure S2, Movie S1).

Multiresponsive Performance. Since aluminum and nitinol are both conductive, the microactuator is connected to a DC power through the contact between the probes and the electrode pads for simple and stable electrical actuation. As another common feature of aluminum and nitinol nanofilms, the rough surfaces allow the microactuator to absorb light and to be actuated through the photothermal mechanism (Figure 2a, Movie S2). This roughness can be observed in the AFM images in Figure S3. We further separately deposited nitinol films and aluminum films in the same thickness and deposition method on wafers for laser absorption tests. The reflectivity of these two films to lasers with different wavelengths was tested in a spectrophotometer. As shown in Figure S4, in the range of visible light (wavelength: 390−780 nm), the reflectivity of nitinol film is 40−45%, and that of the aluminum film is below 1%. To facilitate experimental observations and to increase the absorption of light by both films, a laser with a wavelength of 635 nm was chosen as the driving source and was verified to be effective in heating the actuator (Figure 2d). The modeling of the thermal deformation of the microactuator is established in Section S1 of the Supporting Information.

As the most important index for evaluating the deformation, the projection length of the microactuator is noticed. After applying voltages and lasers, the microactuator contracts and the projection length decreases significantly (Figure 2b). Figure 2c shows the steady states of the microactuator at a range of different driving voltages. As the voltage increases from 0 to 2.5 V, the projection length of the microactuator decreases from 1563.84 to 1294.46 μm (i.e., a 17.2% contraction). During this process, the temperature of the microactuator rises from 22.3 to 50.5 °C, which remains at a relatively low level (Figure 2d). After disconnecting the microactuator with the electrode pads and placing it on the wafer, a similar contraction of the microactuator under lasers was also observed at the same temperature. As the laser power increases from 0 to 500 mW, the projection length of the microactuator decreases from 1422.7 to 1181.03 μm (i.e., a 17.0% contraction). Figure 2e shows that both the projection length and the temperature of the microactuator exhibit a linear response to the laser power, which indicates precise controllability. The response speed of the microactuator is also critical when it comes to biomedicine and robotics applications. Most thermal microactuators and microrobots are limited in terms of response speed mainly due to the slow cooling process. The microrobot in this work is composed of multilayers of ultrathin films with thicknesses of 400−500 nm, promising a pretty high surface-to-volume ratio. According to the Equation S9 in Section S1, the larger the surface-to-volume ratio, the faster the heat dissipation. As shown in Figure 2f, after the laser (power: 500 mW or voltage: 2.5 V) is turned on, the temperature of the microactuator rises from 22.6 to 49.3 °C in 0.24 s. Once the power is cut off, the temperature drops dramatically from 52 to 24.9 °C within 0.11 s and returns completely to room temperature within 2 s (Movie S3), indicating a rapid heating and cooling rate. Movie S4 also shows the rapid response of the microactuator to square-wave voltages of different frequencies. This high-speed response characteristic will enable the microactuator with broader application prospects in biomedicine, and faster speed for microrobots.

Inspired by the inchworm that transforms bending deformation into locomotion in nature, we further study the feasibility of transforming the precise and rapid contraction/expansion deformation of the microactuator into controllable untethered movement. The crawling process of the inchworm can be divided into two steps as shown in Figure 2g. In the initial state, the head and the tail are both fixed. In the first step, the head is fixed and the body is bent to pull the tail forward. Then the tail is fixed and the body is stretched to push the head forward. The same principle is adapted for microrobots in this work. As shown in Figure 2h, after separating the microactuator with the electrode pads from the disconnection part in Figure 1d and placing it on the motion plane (polished silicon wafer surface), the contraction of the microrobot under the irradiation of laser pulls the tail forward. After turning off the laser, the microrobot is stretched to push the head forward. The fixed part of the microrobot is automatically switched in this process because of its asymmetric structural and anisotropic friction. Therefore,
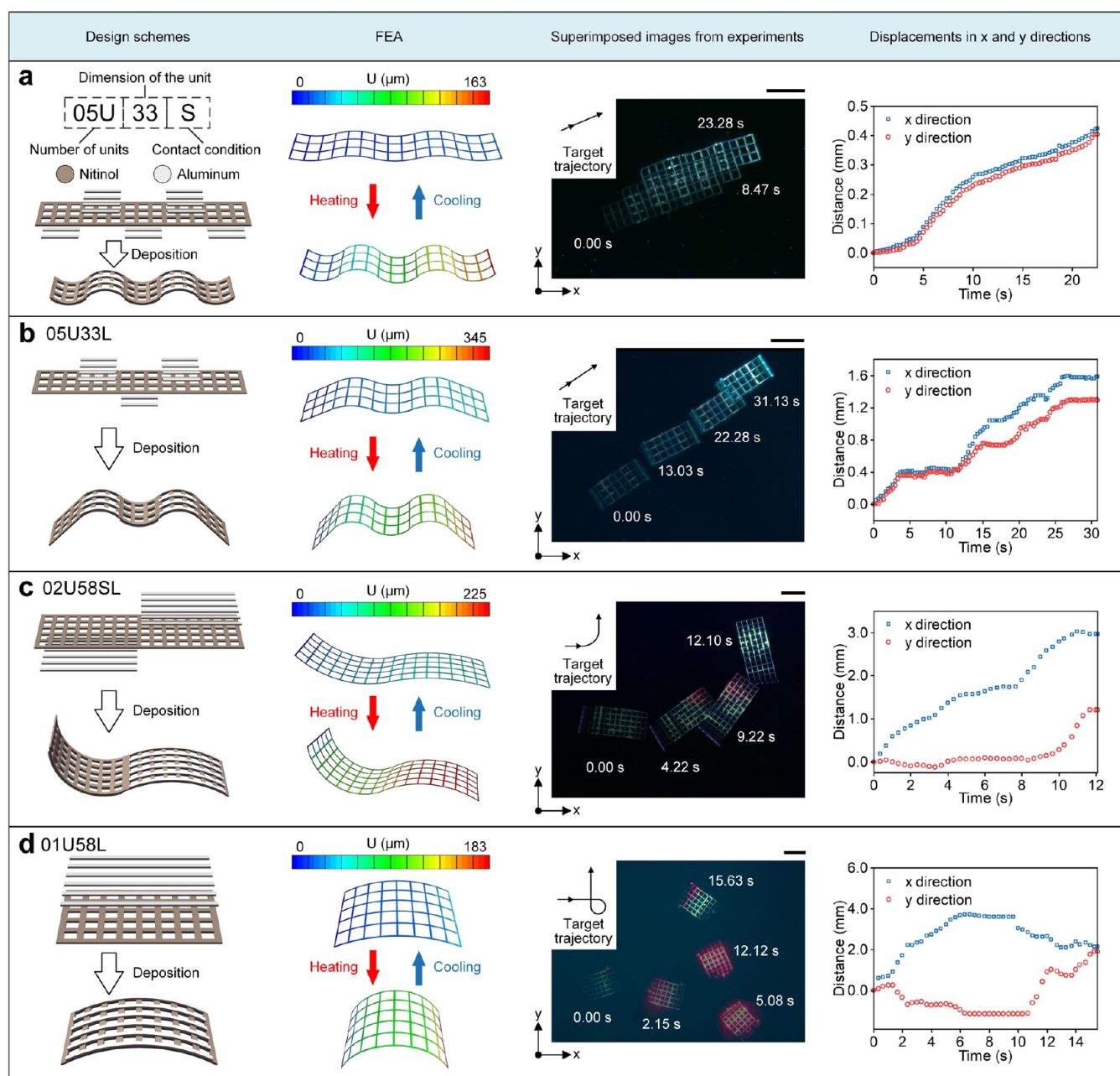
Figure 3. Various microrobots with different 3D configurations. (a) Linear crawling motion of the microrobot 05U33S. (b) Linear crawling motion of the microrobot 05U33L. (c) Turning behaviors of the microrobot 02U58SL induced by the bias laser irradiation. (d) Ultrafast linear crawling, turning, and blocking of the microrobot 01U58L. From left to right: the first column of frames illustrate the exposure view of the microrobots and their 3D structure after fully released. The second column of frames illustrates the FEA results of the microrobots under global heating. The third column of frames illustrates the superimposed images of microrobots of movements. The last column of frames shows displacements along the x and y directions at different time points. Scale bars: 500 μm.

with the periodic irradiation of lasers, the microrobot is able to produce continuous inchworm-type motion (Movie S5). The movement of the microrobot was observed and recorded through a microscope equipped with a CMOS camera. The customized vision-based algorithm described in Figure S5 was applied to analyze the videos for location, displacement, angle, and speed of microrobots.

Various 3D Microrobots. Figure 3a shows the microrobot 05U33S obtained by directly freeing the aforementioned microactuator. Uniform heating creates significant contraction, as verified by FEA (the second frame in Figure 3a). The third frame of Figure 3 shows superposed images during the

movement of the microrobot actuated by a laser (power: 350 mW, frequency: 10 Hz). The average speed of the microrobot reaches 28.2 μm/s. The motion of the microrobot along the x-axis and along the y-axis coincides well, confirming that the robot has a strong ability to maintain its rectilinear motion. The design and microfabrication methods proposed in this work are highly generalizable and scalable. As shown in Figure 3b−d, by changing the 2D layouts of each layer of the film, a variety of microrobots with different configurations can be easily obtained and manufactured simultaneously (Movie S6). Figures S6 and S7 demonstrate the 2D layouts and optical images of these various microrobots. Microrobots with
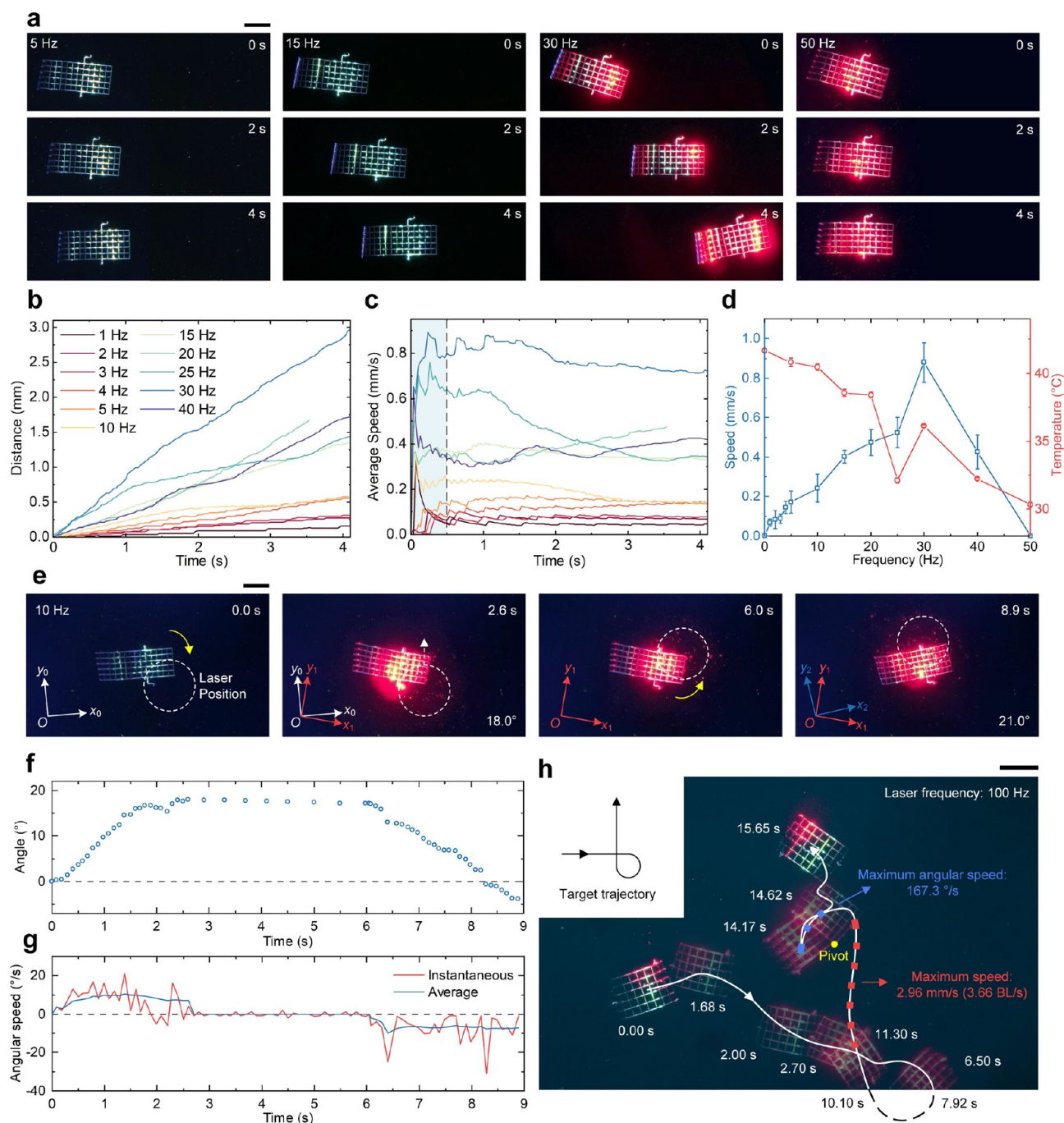
Figure 4. Linear and turning motion. (a) Comparison of the microrobot 02U58SL movement distance under laser frequencies of 5, 15, 30, and 50 Hz in 4 s. (b) Variation of the movement distance under different laser frequencies. (c) Variation of the average speed under different laser frequencies. The initial 0.5 s in the blue area is excluded from the analysis due to the jitter. (d) Speed-temperature-laser frequency graph of the microrobot 02U58SL. (e) Continuous clockwise rotation and counterclockwise rotation of the microrobot by following a 10 Hz moving laser spot. (f) Angle of the microrobot's orientation compared to its initial position changed as a function of time in the rotation progress. (g) Instantaneous and average angular speeds that are obtained by differentiating the data in (f). (h) Controlled movement of the robot 01U58L along a target trajectory. Scale bars: 500 μm.

different configurations have their own characteristics in terms of motion performance. Detailed analyses of these four representative microrobots provide insights into a broad variety of motion patterns that are possible, and how designs and configurations affect motion performance.

Compared with the microrobot 05U33S, the microrobot 05U33L in Figure 3b changes the 2D layout of the lower aluminum film so that the robot "stands up", and the contact condition between the microrobot and the substrates changes from surface contact to line contact. This redesigned configuration helps reduce the slippage and improves the efficiency of the microrobot in converting structural deformation into motion. The average speed of the microrobot 05U33L is 5.1 times (144.4 μm/s) faster than that of the microrobot 05U33S, while the actuation frequency is only about 1/3 of it (laser power: 350 mW, frequency: 3 Hz).
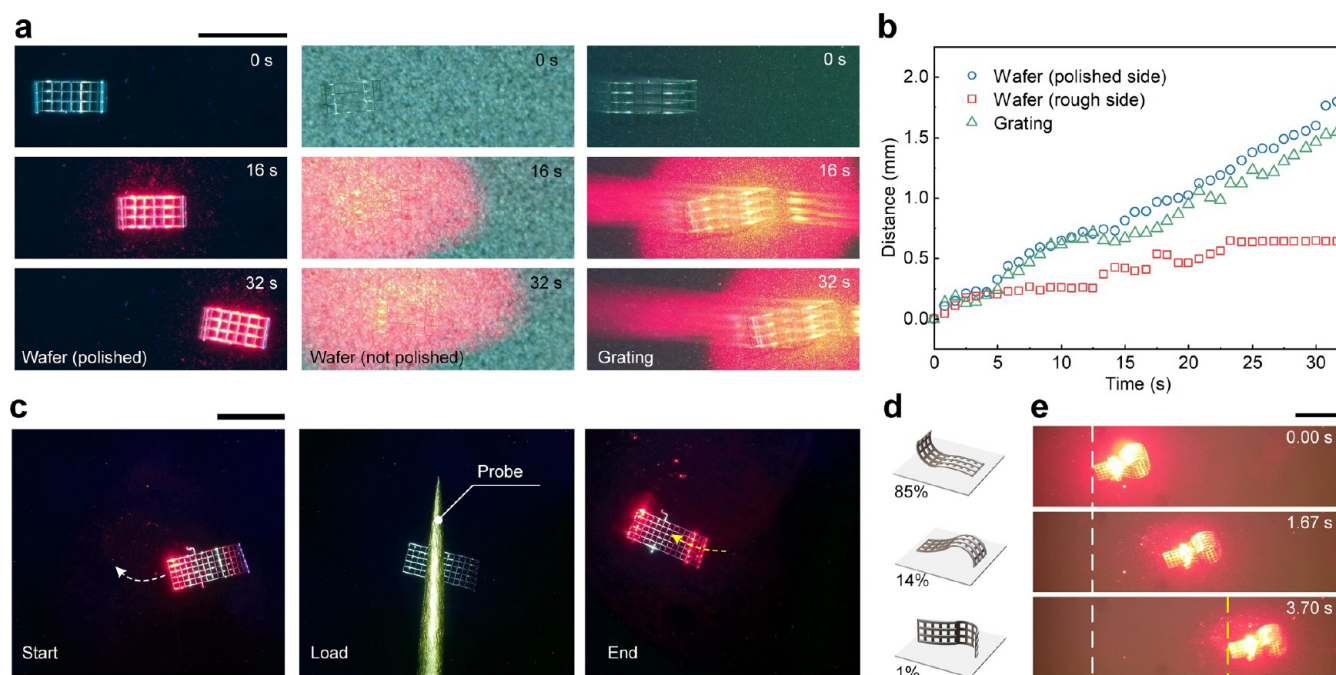
Figure 5. Adaptability and robustness. (a) Comparison of the microrobot movement distance on different substrates including the polished side of the wafer, the rough side of the wafer, and grating in 32 s. (b) Variation in the moving distance of the microrobot on these different substrates. (c) Microrobot can continue to function after being crashed by a probe (50 mg), a load about 67 000-times its own body weight. (d) Definition and statistical results of the three states of the microrobot after free falling. (e) Microrobot moved in a reversed state at a laser frequency of 10 Hz. Scale bars: 1 mm.

However, the line contact condition causes the microrobot 05U33L to be more susceptible to defects on the substrates. It could get stuck during the motion sometimes (5−10 s in the last frame in Figure 3b), and the direction may change slightly (the third frame in Figure 3b).

In order to reduce the slippage between the microrobot and the motion plane, and to enhance the controllability of the motion direction, two more configurations of the microrobot are proposed. Figure 3c presents the microrobot 02U58SL, which consists of two retractable segments. There exist two differentiated contact surfaces between the robot and the motion plane (the front part is in line contact and the rear part is in surface contact with the substrate), which causes anisotropic friction automatically to improve the efficiency of the microrobot to convert structural deformation into motion. Such features allow the microrobots in this work to walk rapidly on ordinary surfaces, unlike many other inchworm-type microrobots that require ratchet surfaces for anisotropic friction to move. The width of the microrobot 02U58SL is wider so that the bias of the laser irradiation on microrobots leads to an asymmetric contraction of the structure for directional movement, improving the motion controllability. As shown in the third frame of Figure 3c, the microrobot rotates counterclockwise with a laser (power: 350 mW, frequency: 30 Hz) irradiating on its left part (the part of the structure illuminated by the laser appears red). The average speeds along the x-axis and the y-axis are 245.4 μm/s and 97.3 μm/s, respectively. The average angular speed is 17.3°/s. The maximum speed of the microrobot 02U58SL reaches 879.3 μm/s (0.59 BL/s) during linear motion. The microrobot 01U58L in Figure 3d is half of the robot 02U58SL. With its even smaller mass and inertia, it is able to convert structural vibration at an even higher frequency (up to 100 Hz) into directional motion and rotation extremely effectively. The

fastest speed in this period of movement reaches 2.96 mm/s (3.66 BL/s), and the maximum angular speed reaches 167.3°/s.

Movement and Rotation Performance. The movement speed of the microrobot is highly correlated with the laser frequency. Figure 4a shows the distance traveled by microrobot 02U58SL in 4 s at different frequencies (5, 15, 30, and 50 Hz). The movement speeds are 57.2 μm/s, 403.1 μm/s, 879.3 μm/s, and 0 μm/s, respectively (Movie S7). Figure 4b and c show the distance and average speed of the robot at different frequencies. In a certain frequency range, the speed of the robot increases as the frequency increases. At low actuation frequencies (1−5 Hz), the motion of the microrobot is relatively stable and continuous. When the actuation frequency exceeds 10 Hz, the motion of the robot begins to fluctuate. At 30 Hz, the robot 02U58SL reaches its maximum speed (879.3 μm/s, 0.59 BL/s). Thereafter, by further increasing the actuation frequency, the speed of the microrobot instead starts to decrease until it is completely immobile. A similar phenomenon can be observed with the microrobot 05U33L. As shown in Figure S8, the movement speeds of the microrobot 05U33L at 1, 3, and 5 Hz are 61.9 μm/s, 142.2 μm/s, and 75.2 μm/s, respectively (Movie S8). Figure 4d concludes the relationship between the speed of the micro-robot 02U58SL and the laser frequency. By measuring the average temperature of the robot at different frequencies, it is found that the main reason for this relationship is that as the actuation frequency increases, the effective heating duration of the laser irradiation during each circle on the microrobot decreases, so as the temperature and the step length. Therefore, under the same conditions, there exists a specific actuation frequency that corresponds to the maximum speed. At its maximum speed of 30 Hz, the microrobot 02U58SL only reaches an average temperature of 36.1 °C, which is harmless
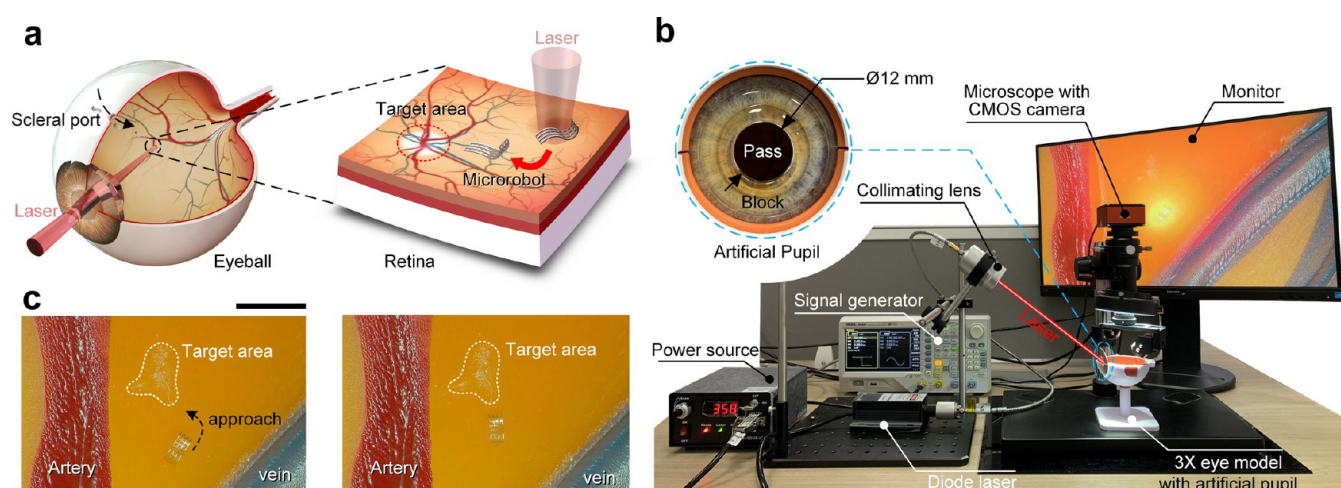
Figure 6. Application demonstration. (a) Concept of the microrobot performing retina surgery under the actuation of a laser. (b) Experimental setup for restricted actuation of the microrobot in a 3X enlarged human eye model. (c) Microrobot addressed and approached the target area under restricted actuation. Scale bars: 1 mm.

to the human body, making it a promising candidate for potential biomedical applications. As shown in Figure S9 and Movie S9, by lifting one side of the wafer, the slope-climbing ability of the microrobot is demonstrated. The microrobot moves at a speed of 643.7 μm/s on the wafer with a slope angle of 6° under the frequency of 30 Hz, which is 73.2% of its normal speed at the same frequency on a horizontal motion plane.

The mechanism of the rotation motion of the microrobots relies on a disequilibrium deformation in the shape of the microrobot under biased laser irradiation. A temperature gradient is formed surrounding the laser spot as shown in Figure S10. Therefore, the bias of the laser irradiation position will lead to an uneven temperature distribution in the structure. By aiming the laser at one side of the robot instead of the center area, an asymmetric contraction will generate a torque perpendicular to the movement plane, leading to a rotation movement. The body coordinate system of the microrobot 02U58SL is defined in Figure 4e, where the x-axis aligns with the longer side of the microrobot. After the laser (power: 350 mW, frequency: 10 Hz) irradiates at the right side, the robot rotates clockwise by 18° in 2.6 s. The laser irradiation point is then moved to the left side, the robot rotates counterclockwise by 21° in 2.9 s. Figure 4f shows the continuous change of the angle of the microrobot during the rotation. The maximum average angular velocity during clockwise and counterclockwise rotations is 10.48°/s and 10.08°/s, respectively (Figure 4g, Movie S10). The angular velocity is also influenced by the laser frequency. The microrobot 02U58SL reaches a maximum angular velocity of 17.34°/s at a laser frequency of 25 Hz (Figure 3c). With the ability to move straightly and turn, the microrobot 01U58L was guided manually along a specific trajectory. As shown in Figure 4h, the fastest speed in this period of movement reached 2.96 mm/s (3.66 BL/s). The microrobot went out of the view at 7.92 s and returned at 10.10 s, with a change in its orientation of 102.6°, which indicated a clockwise rotation of 47.06°/s. At 14.17 s, the right rear part of the microrobot became a pivot point for an ultrafast rotation up to 167.3°/s.

Adaptability and Robustness. The microrobots exhibit excellent adaptability to a variety of motion surfaces. We experimentally demonstrated the movement ability of the

microrobot 05U33L on three different substrates, including the polished side of the wafer, the rough side of the wafer, and grating (300 lines/mm, blazing angle: 27.3°), with different amounts of surface roughness (seen in AFM images in Figure S11). Figure 5a compares the moving distance of the microrobot on these substrates within 32 s. The laser (power: 350 mW, frequency: 1 Hz) used in each case is identical. The average speed of the microrobot on the polished side of the wafer, the rough side of the wafer, and the grating are 52.8 μm/s, 27.8 μm/s, and 48.2 μm/s, respectively (Movie S11). From Figure 5b, it can be seen that the microrobot moves more continuously on the smoother polished side of the wafer. On the other hand, the microrobot gets obstructed sometimes on the rough side of the wafer and the grating and therefore slows down.

The agility, controllability, and adaptability of the microrobot are already demonstrated in the above experiments. In nature, robustness is essential for the survival of creatures. For instance, a cockroach can withstand a load 900 times its body weight without injury.[37] Many primate mammals can still walk while hanging upside down from tree branches to cope with complex survival environments. The above characteristics of these insects and animals come from their physical structure. In practical scenarios, microrobots may face many unexpected risks such as impacts and disturbances. Therefore, robustness is also essential for microrobots to display both fail-safe and fault-tolerant behavior, and to maintain their functionality during the process. The microrobots presented in this work exhibit exceptional robustness characteristics resulting from the simple film structure and approximate symmetrical configuration.

For the fail-safe behavior, the thin-film structure of the microrobot makes it extremely resistant to pressure and impact. As shown in Figure 5c, the microrobot can still return to its original shape and continue to function after being squeezed by a probe (50 mg), a load about 67 000-times its body weight. To experimentally verify the fault-tolerant behavior of the microrobots 02U58SL, we used a bulb syringe to generate omnidirectional airflow to simulate the possible disturbances and unexpected falling the microrobot might face in a practical task environment. After the microrobot is blown up and landed, there are three possible landing state: normal state, reversed state, and side state (Figure 5d, Figure S12,

Movie S12). After 100 blown-up experiments, the microrobot landed in the normal state 85 times, the reversed state 14 times, and the side state only once. For normal states, the movement characteristics have been discussed thoroughly (Figure 4). It cannot be ignored that there is still a considerable chance for the robot to land in the reversed state after falling. When the microrobot 02U58SL is at the reversed state, there remain two different contact surfaces between the robot and substrate to convert contraction/extension deformation into motion. Therefore, it still possesses the ability to move due to its symmetry structure design (Figure 5e, Movie S12). The average speed of the microrobot in the reversed state is around 95% of its speed in the normal state at the same actuation frequency. In the side state, the microrobot loses its movement ability. However, this side state is extremely unstable and can be easily changed to the normal state or the reversed state with slight perturbation. Therefore, when the microrobot faces a sudden disturbance and changes its posture, the probability it can maintain its function is up to 99%, which indicates a strong fault-tolerant ability.

Application Demonstration. With such motion performance, controllability, adaptability, and robustness, the microrobots proposed here will have a promising application prospect in performing precise tasks in restricted scenarios such as retina surgery, where the laser beam can be approached and preferred for direct and precise manipulation in a transparent medium. Figure 6a shows the basic concept of this retina surgery. In this process, the microrobot is small enough to pass a catheter through the scleral port into the vitreum. Then the microrobot will sink to the retina where it will be actuated. Figure 6b experimentally demonstrated how the microrobot can be applied in this restricted scenario where the light path is strictly limited to pass an artificial pupil (diameter: 12 mm) of a 3X enlarged human eye model. The microrobot 05U33L is then guided to a lesion adjacent to the fundus oculi artery (Figure 6c and Movie S13). With the described robustness of the microrobots to external disturbances, a passive obstacle-crossing mechanism is proposed. As shown in Figure S13 and Movie S13, after being blown up by directional airflow, the microrobot 05U33L covered a distance of ~1 cm in only 0.16 s and landed at its normal state, ready for further actuation. In this process, the robot leaped over an artificial artery (an obstacle about 500 μm in height).

Related Works. In nature, arthropods and microorganisms with fast locomotion tend to have advantages in escaping predators and hunting. Similarly, microrobots with fast speed enable them with more application potential for practical scenarios. Figure 7 shows the comparison of relative speeds with respect to body length including several arthropods and microorganisms (green),[38−44] the set of most advanced optical actuated microrobots (orange),[21,28,29,33−36,45−47] inchworm-type microrobots (blue),[30,33,48−52] and this work (red stars). Among inchworm-type microrobots, the microrobots in this work have the smallest size and can operate at a relatively fast speed (3.66 BL/s). This ultrafast speed mainly comes from the advanced 3D structural design and the submillimeter dimensions for fast heat dissipation and high response frequency. Regular microactuators for inchworm-type robotics are limited by their slow response behavior. Those robots who can also move over 1 BL/s require their energy through cable and wire, and therefore are limited in their range of motion and agility.[50,52] Some of them also need extra footpads for friction regulation.[51] Note that our works are the only inchworm-type
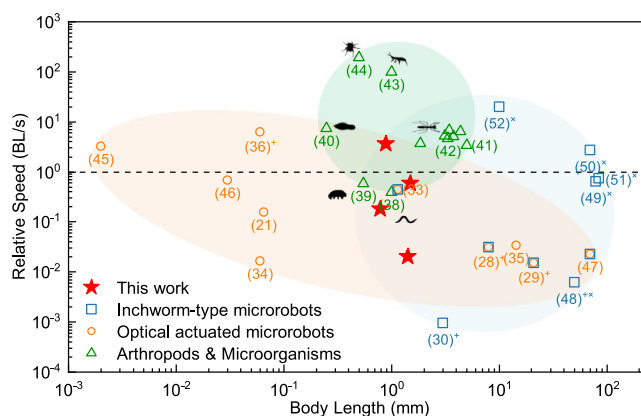

Figure 7. Related works comparison. Summary of reported related microrobots and creatures plotted as the ratio of maximum speed to body length as a function of length. References marked with '+' correspond to robots that need ratchet surfaces to move. References marked with " × " correspond to tethered robots.

microrobots that can move over 1 BL/s while being untethered. For light-actuated robots, the trend in the orange shaded area indicates that the relative speed increases as the body length decreases due to the decrease in robot inertia. However, the modulation of anisotropic friction that drives the motion of microrobots at the microscale becomes very difficult. To address this challenge, most light-actuated microrobots that preserve their characteristics as small size, simple structure, and fast speeds on the requirement of special substrates that present ratchet features or interdigital electrodes.[28,29,36,47] The design and microfabrication method used in this work enables multiple advanced 3D microrobots that allow for differences in robot−substrates contact, automatically achieving anisotropic friction even for conventional surfaces. For artificial microrobots, there is still a long way from the performance of the movement of living creatures in nature. For example, a kind of mite, *Paratarsotomus macropalpis*, with a body length of ~1 mm, can easily reach several hundred body lengths per second with one single jump.[44] In general, the robots in this work is presently the fastest submillimeter robot that can be actuated remotely and move continuously on nonspecialized surfaces. It is faster than some microorganisms such as *Caenorhabditis elegans* (*C. elegans*)[38] and *Tardigrade*[39] of this size, and even comparable to the speed of *Paramecia*[40] and some arthropods in the *Formicidae* family.[41,42]

CONCLUSIONS

In summary, we proposed an electric/light-actuated soft microactuator based on nano bimorph films and developed it into several untethered ultrafast microrobots with exceptional controllability, adaptability, and robustness. Unlike conventional thermal bimorph actuators, this microactuator is composed of multilayer patterned nanofilms and exhibits precise and rapid response under low voltages. The same characteristics reappeared with laser irradiation due to the excellent photothermal effect of the aluminum/nitinol films. These responsive performances enable the microactuator to transform into controllable and fast inchworm-type microrobots actuated by a laser immediately after full freedom. The proposed universal design and microfabrication approach allow us to access various improved and distinctive robotics configurations simultaneously for faster movement and better

controllability. Highly controllable by the laser frequency, the motion speed of the microrobots can reach 2.96 mm/s (3.66 BL/s) on the polished wafer surface. The excellent movement adaptability of the robot is also verified on other rough substrates. Moreover, directional locomotion can be realized simply by the bias of the irradiation of the laser spot, and the maximum angular speed reached 167°/s. Benefiting from the simple bimorph film structure, the microrobot could maintain functionalized after being crashed by a payload 67 000-times heavier than its weight. The microrobot with the symmetrical configuration allowed it to maintain its locomotion even in the reversed state, which realized robustness to resist unexpected disturbances to its posture. In comparison with other reported works and creatures, microrobots in this work are capable of moving over 1 BL/s without ratchet surfaces while being untethered, which makes them comparable to the speed of some arthropods in the *Formicidae* family. These untethered microrobots will have a promising application prospect in biomedicine and other fields.

In future work, the shape memory effect of the nitinol will be further investigated to enhance the jumping ability and load capacity of the microrobot by taking the advantage of its high power density and to expand the application scenarios of the robot through programmable actuation temperature. Automatic programming of the microrobot based on the visual aid system and negative feedback control will also be introduced in the future to improve the control accuracy.

EXPERIMENTAL SECTION

Preparation of the Microactuator and Microrobot. Starting with a 4-in. P-type silicon wafer, the photoresist (AZ5214, Bymicrofab, China) was spin-coated and then exposed to UV light (Figure S1(i−ii)) in a lithography machine (MA6, SUSS, German). The expected patterns on the photoresist were obtained after soaking in the TMAH (tetramethylammonium hydroxide, Runjing Tech, China) for 45 s. 100 nm thick gold film was then deposited (Figure S1(iii)) on the wafer surface by the E-beam evaporation (BS-ITO-600, Branchy, China). To transform the patterns from the photoresist to the gold film, soaking the wafer in the NMP (*N*-methylpyrrolidone, Runjing Tech, China) at 85 °C for 2 h, and then the excess photoresist was lifted off along with the gold on its surface (Figure S1(iv)). Similar processes were repeated to sequentially deposit the patterned lower aluminum (Figure S1(vii)), nitinol (Figure S1(x)), upper aluminum (Figure S1(xiii)), and the SiO$_2$ films (Figure S1(xvi)). In these processes, E-beam evaporation was also used for the deposition of the aluminum film. The magnetron sputtering (Lab-18, Kurt J. Lesker, USA) was used for the deposition of the nitinol film to control the component. The ICPCVD (Plasmalab system 100, Oxford Instruments, UK) was used for the deposition of the SiO$_2$ film for easier liftoff. After etching in the XeF$_2$ atmosphere for 30 min (Xactix E2, SPTS Tech, UK), the microrobot was safely released from the wafer surface and heat-treated at 200 °C for 1 h to automatically transform into the expected 3D shape (Figure S1(xvii)).

Material Characteristic. The SEM images were obtained by a field emission scanning electron microscope (Gemini 500, Zeiss, German). The AFM images were obtained by an atomic force microscope (Dimension Icon, Bruker, German). The reflectivity of the materials to lasers is measured by using a UV/Vis/NIR spectrophotometer (Lambda 1050+, PerkinElmer, USA). The light was directed perpendicular with respect to the surface. The reflected light intensity was estimated by comparing it with the intensity of a Teflon-coated mirror reference.

Optical Actuation System. A diode laser of 635 nm (MRL-III-635−500 mW, Changchun New Industries Optoelectronics Tech, China) was used to actuate the microrobot. The laser passed through an optical fiber and collimating lens for aiming and focusing. The laser

was connected to a signal generator (DG4000, RIGOL Tech, China), which outputs square wave signals to modulate the laser scintillation frequency. The movement of the microrobot was observed and filmed through a digital microscope equipped with the CMOS camera, which would be replaced with an infrared thermometer (AT61M, IRay Technology, China) for temperature measurement.

Motion Analysis. The motion of the microrobot was captured and recorded through a digital microscope equipped with the CMOS camera (MER2−041−436U3C, Daheng Image, China). The recorded video was analyzed using a customized algorithm. Each frame of the video was converted to a grayscale image with an appropriate threshold to highlight the microrobot from the background. A bounding rectangle was calculated to distinguish the contours of the microrobots. Since the centroid of the microrobot coincides with that of the bounding rectangle, the coordinates of the centroid of the bounding rectangle were used to indicate the position of the microrobot. A series of coordinates were obtained by processing all the frames of the video, from which the trajectory and speed of the microrobot were calculated.

ASSOCIATED CONTENT

ⓢ Supporting Information

The Supporting Information is available free of charge at https://pubs.acs.org/doi/10.1021/acsnano.2c12203.

Microactuator modeling; fabrication process flow of the microactuator; optical images of a microrobot standing on the edge of a coin; AFM images of the surface of the films; algorithm to calculate the position and speed of the microrobots; reflectivity of films at different laser wavelengths; superimposed 2D layouts of the microactuators and microrobots; optical images of the microrobots; moving distance of the microrobot at different laser frequencies; slope-climbing ability of the microrobot; temperature distribution at the location of laser irradiation; AFM images of the surface of different movement substrates; different landing states of the microrobots; passive obstacle-crossing of the microrobot (PDF)

Microrobot prototype together with a worker ant (*Tetramorium caespitum*) and a coin for size comparison (MP4)

Contraction/expansion deformation of the microactuator under actuation of electricity and laser (MP4)

Real-time temperature change of the microactuator after the laser is on and off (MP4)

Dynamic response of the microactuator under square wave pulse voltages with the peak voltage of 2.5 V at different frequencies from 1 to 50 Hz (MP4)

Comparison of the motion of an inchworm and a microrobot (MP4)

Movement demonstration of various microrobots with different configurations (MP4)

Movements of the microrobot 02U58SL at different actuation frequencies from 1 to 50 Hz (MP4)

Movements of the microrobot 05U33L at different actuation frequencies from 1 to 3 Hz (MP4)

Slope-climbing ability of the microrobot 02U58SL (MP4)

Clockwise and counterclockwise rotation movement of the microrobot 02U58SL (MP4)

Movements of the microrobot 05U33L on three different substrates (MP4)

Freefalling experiments of the microrobot 02U58SL and its movement at the reversed state (MP4)

Passive obstacle-crossing and target area addressing of the microrobot 05U33L in the 3X enlarged human eye model (MP4)

AUTHOR INFORMATION

Corresponding Author

Jianjun Luo − *School of Aeronautics, Northwestern Polytechnical University, Shaanxi 710072, China;* orcid.org/0000-0002-7865-7155; Email: jjluo@nwpu.edu.cn

Authors

Xusheng Hui − *School of Aeronautics, Northwestern Polytechnical University, Shaanxi 710072, China;* orcid.org/0000-0002-7926-3799

Rong Wang − *School of Aeronautics, Northwestern Polytechnical University, Shaanxi 710072, China*

Hao Sun − *Beijing Advanced Medical Technologies, Ltd. Inc., Beijing 102609, China*

Complete contact information is available at:
https://pubs.acs.org/10.1021/acsnano.2c12203

Author Contributions

X. Hui, J. Luo, and H. Sun conceived the idea. J. Luo supervised the study. X. Hui designed the microactuator and microrobots. X. Hui conducted the experiments with assistance from R. Wang. X. Hui and R. Wang analyzed the data. X. Hui wrote the manuscript. X. Hui, J. Luo, H. Sun, and R. Wang revised the manuscript.

Notes

The authors declare no competing financial interest.

REFERENCES

(1) Kim, B. H.; et al. Three-dimensional electronic microfliers inspired by wind-dispersed seeds. *Nature* **2021**, *597*, 503−510.

(2) Jin, G.; Sun, Y.; Geng, J.; Yuan, X.; Chen, T.; Liu, H.; Wang, F.; Sun, L. Bioinspired soft caterpillar robot with ultra-stretchable bionic sensors based on functional liquid metal. *Nano Energy* **2021**, *84*, 105896.

(3) Sitti, M.; Ceylan, H.; Hu, W.; Giltinan, J.; Turan, M.; Yim, S.; Diller, E. Biomedical applications of untethered mobile milli/microrobots. *Proc. IEEE* **2015**, *103*, 205−224.

(4) Bozuyuk, U.; Yasa, O.; Yasa, I. C.; Ceylan, H.; Kizilel, S.; Sitti, M. Light-triggered drug release from 3D-printed magnetic chitosan microswimmers. *ACS Nano* **2018**, *12*, 9617−9625.

(5) Yim, S.; Sitti, M. Design and rolling locomotion of a magnetically actuated soft capsule endoscope. *IEEE Trans. Robot.* **2012**, *28*, 183−194.

(6) Xie, M.; Zhang, W.; Fan, C.; Wu, C.; Feng, Q.; Wu, J.; Li, Y.; Gao, R.; Li, Z.; Wang, Q.; et al. Bioinspired soft microrobots with precise magneto-collective control for microvascular thrombolysis. *Adv. Mater.* **2020**, *32*, 2000366.

(7) Xin, C.; et al. Environmentally Adaptive Shape-Morphing Microrobots for Localized Cancer Cell Treatment. *ACS Nano* **2021**, *15*, 18048−18059.

(8) Jeon, S.; Park, S. H.; Kim, E.; Kim, J.-y.; Kim, S. W.; Choi, H. A Magnetically Powered Stem Cell-Based Microrobot for Minimally Invasive Stem Cell Delivery via the Intranasal Pathway in a Mouse Brain. *Adv. Healthcare Mater.* **2021**, *10*, 2100801.

(9) Qiu, F.; Fujita, S.; Mhanna, R.; Zhang, L.; Simona, B. R.; Nelson, B. J. Magnetic helical microswimmers functionalized with lipoplexes for targeted gene delivery. *Adv. Funct. Mater.* **2015**, *25*, 1666−1671.

(10) Wu, Z.; Li, L.; Yang, Y.; Hu, P.; Li, Y.; Yang, S.-Y.; Wang, L. V.; Gao, W. A microrobotic system guided by photoacoustic computed tomography for targeted navigation in intestines in vivo. *Sci. Robot.* **2019**, *4*, No. eaax0613.

(11) Leong, T. G.; Randall, C. L.; Benson, B. R.; Bassik, N.; Stern, G. M.; Gracias, D. H. Tetherless thermobiochemically actuated microgrippers. *Proc. Natl. Acad. Sci. U. S. A.* **2009**, *106*, 703−708.

(12) Nelson, B. J.; Kaliakatsos, I. K.; Abbott, J. J. Microrobots for minimally invasive medicine. *Annu. Rev. Biomed. Eng.* **2010**, *12*, 55−85.

(13) Jeon, S.; Hoshiar, A. K.; Kim, K.; Lee, S.; Kim, E.; Lee, S.; Kim, J.-y.; Nelson, B. J.; Cha, H.-J.; Yi, B.-J.; Choi, H. A magnetically controlled soft microrobot steering a guidewire in a three-dimensional phantom vascular network. *Soft Robot* **2019**, *6*, 54−68.

(14) Zhang, H.; Li, Z.; Gao, C.; Fan, X.; Pang, Y.; Li, T.; Wu, Z.; Xie, H.; He, Q. Dual-responsive biohybrid neutrobots for active target delivery. *Sci. Robot.* **2021**, *6*, No. eaaz9519.

(15) Ullrich, F.; Bergeles, C.; Pokki, J.; Ergeneman, O.; Erni, S.; Chatzipirpiridis, G.; Pané, S.; Framme, C.; Nelson, B. J. Mobility experiments with microrobots for minimally invasive intraocular surgery. *Invest. Ophthalmol. Visual Sci.* **2013**, *54*, 2853−2863.

(16) Xiao, M.; Jiang, C.; Shi, F. Design of a UV-responsive microactuator on a smart device for light-induced ON-OFF-ON motion. *NPG Asia Mater.* **2014**, *6*, No. e128.

(17) Dillinger, C.; Nama, N.; Ahmed, D. Ultrasound-activated ciliary bands for microrobotic systems inspired by starfish. *Nat. Commun.* **2021**, *12*, 1−11.

(18) Luo, T.; Wu, M. Biologically inspired micro-robotic swimmers remotely controlled by ultrasound waves. *Lab Chip* **2021**, *21*, 4095−4103.

(19) Tottori, S.; Zhang, L.; Qiu, F.; Krawczyk, K. K.; Franco-Obregón, A.; Nelson, B. J. Magnetic helical micromachines: fabrication, controlled swimming, and cargo transport. *Adv. Mater.* **2012**, *24*, 811−816.

(20) Huang, H.-W.; Uslu, F. E.; Katsamba, P.; Lauga, E.; Sakar, M. S.; Nelson, B. J. Adaptive locomotion of artificial microswimmers. *Sci. Adv.* **2019**, *5*, No. eaau1532.

(21) Kim, M.-S.; Lee, H.-T.; Ahn, S.-H. Laser Controlled 65 Micrometer Long Microrobot Made of Ni-Ti Shape Memory Alloy. *Adv. Mater. Technol.* **2019**, *4*, 1900583.

(22) Lee, H.-T.; Kim, M.-S.; Lee, G.-Y.; Kim, C.-S.; Ahn, S.-H. Shape memory alloy (sma)-based microscale actuators with 60% deformation rate and 1.6 kHz actuation speed. *Small* **2018**, *14*, 1801023.

(23) Hu, Y.; Yang, L.; Yan, Q.; Ji, Q.; Chang, L.; Zhang, C.; Yan, J.; Wang, R.; Zhang, L.; Wu, G.; Sun, J.; Zi, B.; Chen, W.; Wu, Y. Self-Locomotive Soft Actuator Based on Asymmetric Microstructural Ti3C2T x MXene Film Driven by Natural Sunlight Fluctuation. *ACS Nano* **2021**, *15*, 5294−5306.

(24) Xiao, X.; Ma, H.; Zhang, X. Flexible Photodriven Actuator Based on Gradient−Paraffin-Wax-Filled Ti3C2T x MXene Film for Bionic Robots. *ACS Nano* **2021**, *15*, 12826−12835.

(25) Wang, M.; Zhou, L.; Deng, W.; Hou, Y.; He, W.; Yu, L.; Sun, H.; Ren, L.; Hou, X. Ultrafast Response and Programmable Locomotion of Liquid/Vapor/Light-Driven Soft Multifunctional Actuators. *ACS Nano* **2022**, *16*, 2672−2681.

(26) Zheng, J.; Xiao, P.; Le, X.; Lu, W.; Théato, P.; Ma, C.; Du, B.; Zhang, J.; Huang, Y.; Chen, T. Mimosa inspired bilayer hydrogel actuator functioning in multi-environments. *J. Mater. Chem. C* **2018**, *6*, 1320−1327.

(27) Zhang, Z.; Chen, Z.; Wang, Y.; Chi, J.; Wang, Y.; Zhao, Y. Bioinspired bilayer structural color hydrogel actuator with multi-environment responsiveness and survivability. *Small Methods* **2019**, *3*, 1900519.

(28) Zeng, H.; Wani, O. M.; Wasylczyk, P.; Priimagi, A. Light-driven, caterpillar-inspired miniature inching robot. *Macromol. Rapid Commun.* **2018**, *39*, 1700224.

(29) Shahsavan, H.; Aghakhani, A.; Zeng, H.; Guo, Y.; Davidson, Z. S.; Priimagi, A.; Sitti, M. Bioinspired underwater locomotion of light-driven liquid crystal gels. *Proc. Natl. Acad. Sci. U. S. A.* **2020**, *117*, 5125−5133.

(30) Maeda, S.; Hara, Y.; Sakai, T.; Yoshida, R.; Hashimoto, S. Self-walking gel. *Adv. Mater.* **2007**, *19*, 3480−3484.

(31) Hui, X.; Luo, J.; Wang, X.; Wang, R.; Sun, H. Bimorph electrothermal micro-gripper with large deformation, precise and rapid response, and low operating voltage. *Appl. Phys. Lett.* **2022**, *121*, 023502.

(32) Wang, W.; Xiang, C.; Zhu, Q.; Zhong, W.; Li, M.; Yan, K.; Wang, D. Multistimulus responsive actuator with GO and carbon nanotube/PDMS bilayer structure for flexible and smart devices. *ACS Appl. Mater. Interfaces* **2018**, *10*, 27215−27223.

(33) Han, M.; et al. Submillimeter-scale multimaterial terrestrial robots. *Sci. Robot.* **2022**, *7*, No. eabn0602.

(34) Miskin, M. Z.; Cortese, A. J.; Dorsey, K.; Esposito, E. P.; Reynolds, M. F.; Liu, Q.; Cao, M.; Muller, D. A.; McEuen, P. L.; Cohen, I. Electronically integrated, mass-manufactured, microscopic robots. *Nature* **2020**, *584*, 557−561.

(35) Rogóż, M.; Zeng, H.; Xuan, C.; Wiersma, D. S.; Wasylczyk, P. Light-driven soft robot mimics caterpillar locomotion in natural scale. *Adv. Opt. Mater.* **2016**, *4*, 1689−1694.

(36) Zeng, H.; Wasylczyk, P.; Parmeggiani, C.; Martella, D.; Burresi, M.; Wiersma, D. S. Light-fueled microscopic walkers. *Adv. Mater.* **2015**, *27*, 3883−3887.

(37) Wu, Y.; Yim, J. K.; Liang, J.; Shao, Z.; Qi, M.; Zhong, J.; Luo, Z.; Yan, X.; Zhang, M.; Wang, X.; Fearing, R. S.; Full, R. J.; Lin, L. Insect-scale fast moving and ultrarobust soft robot. *Sci. Robot.* **2019**, *4*, No. eaax1594.

(38) Jung, J.; Nakajima, M.; Takeuchi, M.; Najdovski, Z.; Huang, Q.; Fukuda, T. Microfluidic device to measure the speed of C. elegans using the resistance change of the flexible electrode. *Micromachines* **2016**, *7*, 50.

(39) Nirody, J. A.; Duran, L. A.; Johnston, D.; Cohen, D. J. Tardigrades exhibit robust interlimb coordination across walking speeds and terrains. *Proc. Natl. Acad. Sci. U. S. A.* **2021**, *118*, No. e2107289118.

(40) Shunmugam, A. P.; Subramanian, G.; Fernandez, J. G. Measurements of the swimming speeds of motile microorganisms using object tracking and their correlation with water pollution and rheology levels. *Sci. Rep.* **2021**, *11*, 1−8.

(41) Duncan, F.; Crewe, R. A comparison of the energetics of foraging of three species of Leptogenys (Hymenoptera, Formicidae). *Physiol. Entomol.* **1993**, *18*, 372−378.

(42) Pearce-Duvet, J. M.; Elemans, C. P.; Feener, D. H., Jr Walking the line: search behavior and foraging success in ant species. *Behav. Ecol.* **2011**, *22*, 501−509.

(43) Brackenbury, J.; Hunt, H. Jumping in springtails: mechanism and dynamics. *J. Zool.* **1993**, *229*, 217−236.

(44) Rubin, S.; Young, M. H.-Y.; Wright, J. C.; Whitaker, D. L.; Ahn, A. N. Exceptional running and turning performance in a mite. *J. Exp. Biol.* **2016**, *219*, 676−685.

(45) Wu, X.; Ehehalt, R.; Razinskas, G.; Feichtner, T.; Qin, J.; Hecht, B. Light-driven microdrones. *Nat. Nanotechnol.* **2022**, *17*, 477−484.

(46) Sul, O.; Falvo, M.; Taylor, R.; Washburn, S.; Superfine, R. Thermally actuated untethered impact-driven locomotive micro-devices. *Appl. Phys. Lett.* **2006**, *89*, 203512.

(47) Wang, X.-Q.; Chan, K. H.; Cheng, Y.; Ding, T.; Li, T.; Achavananthadith, S.; Ahmet, S.; Ho, J. S.; Ho, G. W. Somatosensory, light-driven, thin-film robots capable of integrated perception and motility. *Adv. Mater.* **2020**, *32*, 2000351.

(48) Sun, Y.-C.; Leaker, B. D.; Lee, J. E.; Nam, R.; Naguib, H. E. Shape programming of polymeric based electrothermal actuator (ETA) via artificially induced stress relaxation. *Sci. Rep.* **2019**, *9*, 1−12.

(49) Chi, Y.; Tang, Y.; Liu, H.; Yin, J. Leveraging Monostable and Bistable Pre-Curved Bilayer Actuators for High-Performance Multi-task Soft Robots. *Adv. Mater. Technol.* **2020**, *5*, 2000370.

(50) Tang, Y.; Chi, Y.; Sun, J.; Huang, T.-H.; Maghsoudi, O. H.; Spence, A.; Zhao, J.; Su, H.; Yin, J. Leveraging elastic instabilities for amplified performance: Spine-inspired high-speed and high-force soft robots. *Sci. Adv.* **2020**, *6*, No. eaaz6912.

(51) Gu, G.; Zou, J.; Zhao, R.; Zhao, X.; Zhu, X. Soft wall-climbing robots. *Sci. Robot.* **2018**, *3*, No. eaat2874.

(52) Liang, J.; Wu, Y.; Yim, J. K.; Chen, H.; Miao, Z.; Liu, H.; Liu, Y.; Liu, Y.; Wang, D.; Qiu, W.; Shao, Z.; Zhang, M.; Wang, X.; Zhong, J.; Lin, L. Electrostatic footpads enable agile insect-scale soft robots with trajectory control. *Sci. Robot.* **2021**, *6*, No. eabe7906.